ChemPubSoc Europe

DOI: 10.1002/chem.201800694

CHEMISTRY A European Journal Full Paper

Metal-organic frameworks

Metal-Organic Frameworks as Catalyst Supports: Influence of Lattice Disorder on Metal Nanoparticle Formation

Miguel Rivera-Torrente,[a] Matthias Filez,[a] Rifan Hardian,[b] Emily Reynolds,[c] Beatriz Seoane,[a] Marie-Vanessa Coulet,[b] Freddy E. Oropeza Palacio,[d] Jan P. Hofmann,[d] Roland A. Fischer,[e, f] Andrew L. Goodwin,[c] Philip L. Llewellyn,[b] and Bert M. Weckhuysen*[a]

Abstract: Because of their high tunability and surface area, metal-organic frameworks (MOFs) show great promise as supports for metal nanoparticles. Depending on the synthesis route, MOFs may contain defects. Here, we show that highly crystalline MIL-100(Fe) and disordered Basolite® F300, with identical iron 1,3,5-benzenetricarboxylate composition, exhibit very divergent properties when used as a support for Pd nanoparticle deposition. While MIL-100(Fe) shows a regular MTN-zeotype crystal structure with two types of cages, Basolite® F300 lacks long-range order beyond 8 Å and has a single-pore system. The medium-range configurational linker-node disorder in Basolite® F300 results in a reduced number of Lewis acid sites, yielding more hydrophobic surface properties compared to hydrophilic MIL-100(Fe). The hydrophilic/hydrophobic nature of MIL-100(Fe) and Basolite® F300 impacts the amount of Pd and particle size distribution of Pd nanoparticles deposited during colloidal synthesis and dry impregnation methods, respectively. It is suggested that polar (apolar) solvents/precursors attractively interact with hydrophilic (hydrophobic) MOF surfaces, allowing tools at hand to increase the level of control over, for example, the nanoparticle size distribution.

Introduction

Metal-organic frameworks (MOFs) are a relatively new family of porous compounds, which consist of metal nodes interconnected by organic linkers forming a crystalline network with potential voids.[1] By varying the metal and linker type, the MOF properties can be altered and their pore space modified according to functional and diffusional needs. This tunability, together with exceptionally high specific surface areas and very rich post- and pre-synthetic chemistries, has generated keen interest within the scientific community, and MOFs have become the target of intense research. One particular function for which MOFs show strong potential is as hosts for metal nanoparticles in a diverse set of applications, ranging from chemical sensing,[2] to gas storage,[3] and catalysis.[4] Indeed, MOFs have emerged as an attractive alternative to classic heterogeneous metal oxide or carbon supports, owing to their structural variability, opening the way for the synthesis of application-tailored supports.[5] However, despite the potential of MOFs as porous supports, the initial solvent wettability, transport, and anchoring of the metal precursors on the MOF surface, as well as subsequent metal nanoparticle (NP) formation, are not well-understood and impede control over the nanoparticle properties and stability.[6]

Defect engineering is becoming an increasingly important discipline in MOF science.[7] Whether it is by targeted introduction or natural occurrence, the presence of disordered domains may perturb the original MOF framework, thereby influencing the pore structure.[8] When it comes to the use of MOFs as supports, the presence of these disordered domains has the po-

[a] M. Rivera-Torrente, Dr. M. Filez, Dr. B. Seoane, Prof. B. M. Weckhuysen
Inorganic Chemistry and Catalysis
Debye Institute for Nanomaterials Science, Utrecht University
Universiteitsweg 99, 3584 CG Utrecht (The Netherlands)
E-mail: b.m.weckhuysen@uu.nl

[b] R. Hardian, Dr. M.-V. Coulet, Prof. P. L. Llewellyn
Aix-Marseille University
CNRS, MADIREL (UMR 7246)
Centre de St Jérôme, 13013 Marseille Cedex (France)

[c] Dr. E. Reynolds, Prof. A. L. Goodwin
Department of Chemistry, University of Oxford
Inorganic Chemistry Laboratory
South Parks Road, Oxford OX1 3QR (United Kingdom)

[d] Dr. F. E. Oropeza Palacio, Dr. J. P. Hofmann
Laboratory of Inorganic Materials Chemistry
Department of Chemical Engineering and Chemistry
Eindhoven University of Technology, PO Box 513, 5600 MB Eindhoven (The Netherlands)

[e] Prof. R. A. Fischer
Department of Chemistry, Technische Universität München
Lichtenbergstraße 4, 85748 Garching (Germany)

[f] Prof. R. A. Fischer
Catalysis Research Centre, Technische Universität München
Ernst-Otto-Fischer Straße 1, 85748 Garching (Germany)

Supporting information and the ORCID identification number(s) for the author(s) of this article can be found under: https://doi.org/10.1002/chem.201800694.

tential to play a key role.[9] For example, the introduction of disorder may result in mesopore formation, which allows for a more rapid diffusion of liquids or gases. Furthermore, Lewis (M^{n+}) and Brønsted acid -OH and -COOH groups can arise from linker defects or adsorbed molecules on exposed metal sites.[9,10] Nonetheless, up to now, the effect of disorder when using a MOF as a support for metal nanoparticles has not been investigated in great detail, hampering the use of defect engineering as a synthetic tool for the rational design of NP deposition.

In this study, our goal is to gain insight into the impact of the lattice disorder on metal deposition and NP formation in MOF hosts. In particular, our study focuses on the use of two different supports: 1) defect-free MIL-100(Fe), possessing the MTN (named after Socony Mobil Thirty-Nine) zeolite framework type, and 2) its non-crystalline Basolite® F300 analogue,[11] containing structural defects (such as kinks, grain boundaries, cracks, or voids) owing to the synthesis protocol used for its preparation.[12] In order to understand how structural spatial arrangement modifies physico-chemical properties, a wide variety of spectroscopic and textural characterization methods have been applied on both defect-free MIL-100(Fe) and disordered Basolite® F300. Based on this, a more complete picture, as schematically shown in Figure 1 a, emerges on the structure and properties of these two materials. Thereafter, impregnation of different Pd metal precursors, as well as deposition of colloidal nanoclusters, has been carried out, so as to shed light on the effect of MOF lattice disorder on metal NP deposition.

It will be shown that the disordered framework of MOF materials, that is, non-periodic ordering of metal nodes and organic linkers, has a strong impact on surface polarity. Thus, the Pd content, the Pd NP size, and related distribution within the MOF material can be rationalized accordingly, and is shown to be dependent on the precursor- and solvent-type, as a result of support surface polarity, as outlined in Figure 1 b.

Results and Discussion

To gain new insight into the role of disorder on the use of MOFs as catalyst supports, two MOFs have been selected as hosts to deposit Pd NPs, namely, 1) lab-synthesized non-defective MIL-100(Fe) and 2) commercial non-crystalline Basolite® F300 iron 1,3,5-benzenetricarboxylate. As described below, these materials have similar iron 1,3,5-benzenetricarboxylate composition (although the molecular formula of Basolite® F300 remains unknown), yet their properties differ significantly. Thereafter, Pd nanoparticles are introduced following: 1) incipient wetness impregnation, and 2) colloidal deposition, as shown in Figure 1 b.

Materials characterization

Crystallinity. Powder X-ray diffraction (PXRD) of MIL-100(Fe) and Basolite® F300 supports shows a sharp contrast in structural order at longer length ranges. In the case of MIL-100(Fe), that crystallizes in a face-centered cubic FCC structure of the $Fd\bar{3}m$ group, XRD displays sharp diffraction peaks at 2.4°, 3.9°,

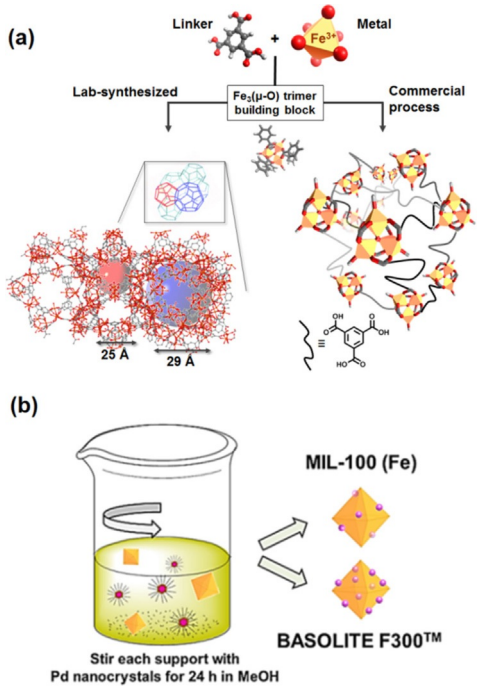

Figure 1. (a) Schematic representation of the different materials obtained from a Fe^{3+} source and trimesic acid (H_3BTC). Depending on the synthesis conditions, either highly crystalline MIL-100(Fe) or disordered, porous iron (III) 1,3,5-benzenetricarboxylate can be obtained, with the subsequent change in properties. (b) Schematic representation of the colloidal deposition experiments resulting in different Pd/Fe-BTC materials.

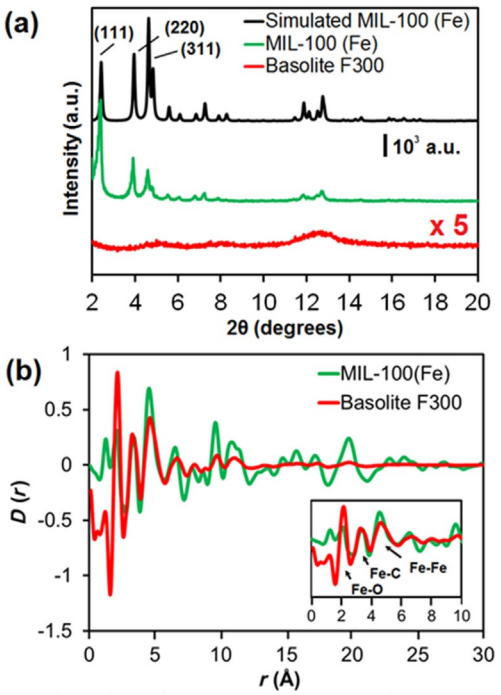

Figure 2. (a) PXRD and (b) normalized probability $D(r)$ obtained from X-ray total scattering of (green) MIL-100(Fe) and (red) Basolite® F300 supports. Inset shows first, second and third coordination shells together with the corresponding assigned bonds.

and 4.6°, corresponding to the (111), (220), and (311) crystallographic planes of MIL-100(Fe), respectively (Figure 2a). This indicates that the synthesized material indeed has the MTN-zeotype architecture. On the other hand, Basolite® F300 presents a smooth pattern, in contrast to previous literature,[12a] characteristic of non-crystalline solid, thus preventing the assignment to a given crystalline structure. To further understand MIL-100(Fe) and Basolite® F300 structure at the short and intermediate range, X-ray Pair Distribution Function (XPDF) analysis was conducted on both materials. The local environment of Fe atoms in MIL-100(Fe) and Basolite® F300 show very similar first (Fe–O), second (Fe–C), and third (Fe–Fe) coordination shells (Figure 2b). The lengths of the Fe–O bond are 2.08 and 2.12 Å for MIL-100(Fe) and Basolite® F300, respectively. Further, Fe–C and Fe–Fe distances were measured to be 3.4 and 3.2 Å; and 4.6 and 4.5 Å, for MIL-100(Fe) and Basolite® F300, respectively. These similar atom distances suggest minor structural changes between both materials in the first 3 coordination shells around Fe atoms.[13]

However, the structural arrangement at intermediate and long ranges differs strongly from one support to the other. Beyond ca. 8 Å, Basolite® F300 shows very low PDF intensity, which corroborates the lack of long-range order, as observed in PXRD. MIL-100(Fe) on the other hand shows intense signal features. Collectively, these results show that both MIL-100(Fe) and Basolite® F300 possess, at the local scale, oxo-centered trimers of iron octahedra. These, however, are assembled through BTC ligands into a disordered lattice, with structural amorphization at length scales beyond the trimer building block. Therefore, we can conclude that Basolite® F300 is structurally perturbed compared to the highly ordered MIL-100(Fe). Additional Raman spectroscopy reveals that the band intensity ratio of 1606 cm^{-1} ν(C=C) to 1550 cm^{-1} $\nu(O–C–O)_{asymmetric}$ is higher for Basolite® F300 compared to MIL-100(Fe) (Figure S1 in Supporting Information).[14] This suggests that O-C-O bond vibrations are less intense for disordered Basolite® F300, as a consequence of increased O-C-O bond disorder due to structural perturbation. This further suggests that structural disorder affects bond vibrations.

Porosity. MOF framework crystallinity, or the lack thereof, has a potential impact on the pore network geometry. N_2 isotherms acquired at 77 K (Figure 3a) showed a type I behavior for both crystalline MIL-100(Fe) and disordered Basolite® F300, typical of microporous materials. This implies that no meso- and macroporosity is introduced in Basolite® F300 due to perturbed metal-linker organization. Aside from their similar isotherm type, multiple differences are present between both materials. First, the MIL-100(Fe) and Basolite® F300 BET surface areas amount to 1040 and 685 $m^2 g^{-1}$, respectively. Owing to the difference in synthetic protocols, the surface area of MIL-100(Fe) differs from the one reported by the group of Férey, suggesting not as well crystallized material (also observed in XRD peak broadness).[15] Even though Férey and co-workers have reported MIL-100(Fe) with even higher crystallinity, here we aim to compare MIL-100(Fe), obtained by simple and scalable synthesis protocols that do not involve the presence of HF, to Basolite® F300.

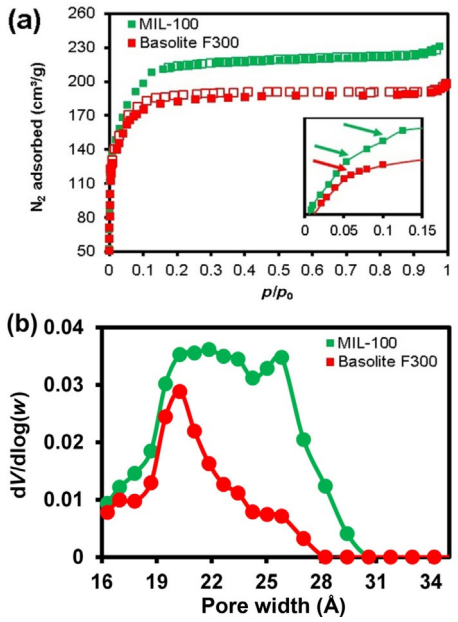

Figure 3. (a) N_2 adsorption isotherm at 77 K (inset shows the low-pressure $p/p_0 \leq 0.015$ range with different steps indicated by the arrows) and (b) pore size distribution of both materials derived from the N_2 adsorption data by the NLDFT method, that was used here to get a simple estimate of the pore size distribution. Arrows indicate each type of cage in the structure corresponding to the steps in the isotherm.

In addition, their respective pore volumes differ from 0.45 $cm^3 g^{-1}$ for MIL-100(Fe) to 0.29 $cm^3 g^{-1}$ for Basolite® F300. Therefore, the overall loss in crystallinity observed for Basolite® F300 relative to MIL-100(Fe) causes a decrease in the porosity of these microporous materials. This porosity loss is also reflected in the maximal N_2 uptake at $p/p_0 > 0.95$ which decreases from 220 $cm^3 g^{-1}$ for MIL-100(Fe) to 190 $cm^3 g^{-1}$ for Basolite® F300. A detailed investigation of the MIL-100(Fe) isotherm in the low relative pressure regime—p/p_0 between 0.05 and 0.15—shows two steps, corresponding to the filling of the two different cages (Figure 3a inset).[15] As the experimentally determined pore size of MIL-100(Fe) is reported to be in the limit between micro and mesopore,[16] the use of non-local density functional theory (NLDFT) to evaluate the pore size distribution is considered to be the best method compared to the Barrett–Joyner–Halenda (BJH) method that is applicable only for mesoporous materials. The challenge in the NLDFT method, however, is that no perfect kernels are known for MOFs. In this study, we considered to apply NLDFT with a model of nitrogen on silica with cylindrical pore, as it shows the best result. Indeed, our results are comparable to previous reports that used DFT methods.

As can be observed, the overall loss in crystallinity observed for Basolite® F300 relative to MIL-100(Fe) causes a decrease in the porosity of these materials. The loss of porosity in Basolite® F300 may also affect the acidity and hydrophilicity of the material that will be further discussed. The estimated NLDFT pore size distribution of MIL-100(Fe) exhibits a bimodal shape, where the two modi are centered at ≈18–23 Å and ≈25–27 Å (Figure 3b), corresponding to the two cages of the zeotypic structure.

In contrast, Basolite® F300 exhibits a single visually observable step in the low-pressure regime. Estimation of the pore size distribution logically yields a monomodal pore size distribution, centered around 18–22 Å, though with lower abundances relative to MIL-100(Fe). This suggests that the bimodal pore system of MIL-100(Fe) is not present in Basolite® F300, possibly due to the disordered nature of this compound.

Acidity. The Basolite® F300 structure is strongly perturbed compared to the crystalline MIL-100(Fe), yielding a lack of long range order beyond 8 Å and well-defined pore network. Whilst order in the pore system may not be a requirement for many applications, such configurationally perturbed linker-node organization can induce changes in the acidic properties of these materials, which is substantiated here by probe-molecule Fourier-transformed infrared spectroscopy (FTIR). Prior to pyridine-probed (Py) FTIR, the supports were dried at 498 K under secondary vacuum ($p < 10^{-3}$ mbar) for 16 h to remove terminal aqua and hydroxido ligands bound to Fe^{3+} Lewis acid coordinatively unsaturated sites (CUS).[18] The Py FTIR spectra show two main bands at 1070 and 1042 cm^{-1}, corresponding to the ν_{18a} and ν_{12} asymmetrical ring-stretching modes of pyridine, respectively (Figure 4a).[19] No shifts are observed after prolonged pyridine exposure in any of the samples, indicating no interaction with the MOF surface affecting those modes. The band at 1014 cm^{-1} corresponds to pyridine interacting with Fe^{3+} sites, that is, Py···Fe^{3+}, whereas the band at 1007 cm^{-1} relates to reduced Fe^{2+} centers.[17] Evolution of the normalized intensity of the band at 1042 cm^{-1} over time (Figure S2) reveals that pyridine uptake reaches a steady state for Basolite® F300 after 30 min, while it increases linearly up to 60 min in the case of MIL-100(Fe). This indicates that a higher amount of pyridine can be adsorbed, suggesting that there are more adsorption sites per unit surface area, thus, a higher number of acid sites in the case of MIL-100(Fe). Moreover, the relative intensity of the bands at 1014 and 1007 cm^{-1} is different at similar adsorption times. This indicates that the redox properties of Fe sites are different for each MOF, as previously reported by the group of García.[20] They might be associated to steric or electronic constraints particular to each material, although further experiments would be necessary to elucidate them.

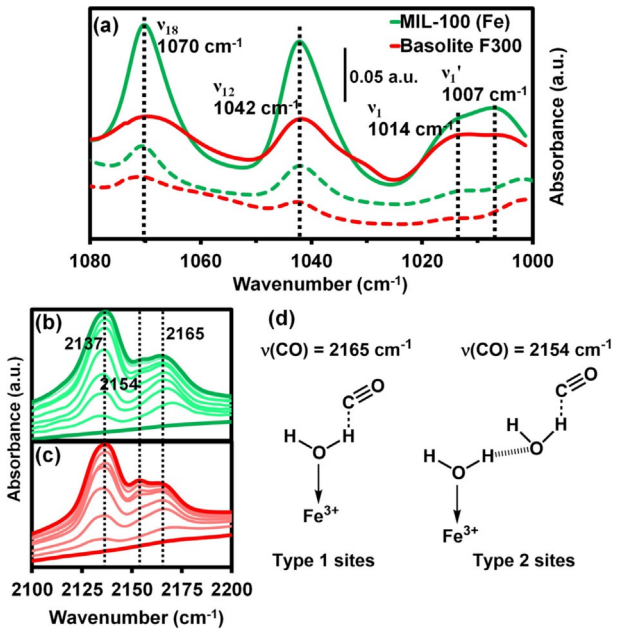

Figure 4. FTIR spectra showing the 1100-1000 cm^{-1} region of (green) MIL-100(Fe) and (red) Basolite® F300 1 min and 60 min after introducing 15 mbar of pyridine at 323 K. Spectra were recorded in transmission mode on ≈10 mg pellets. (b) Basolite® F300 and (c) MIL-100(Fe) at different CO pressures (from 10^{-2} mbar to 100 mbar) at 85 K. (d) Schematic representation of the vibrational modes assigned to the bands of CO bonded to different H_2O-Fe^{3+} species and physisorbed CO (2137 cm^{-1}), adapted from Ref [17].

Dhakshinamoorthy et al.[20] observed a correlation in intensity between the ν_1 mode at 1007 cm^{-1} and the sharp ν(OH) vibrational band at 3575 cm^{-1}, assigned to the free carboxylic groups (both from unreacted trimesic acid and point defects), which they connected to PyH^+ sites of -OH groups arising from those defects and impurities. In our study, the band at 1007 cm^{-1} was observed in the spectra of both materials after pyridine dosing, but no effect on the 2000–3600 cm^{-1} region was observed. This implies that both materials have a certain amount of reduced Fe^{2+} sites, but no significant amount of linker defects are observed. When comparing the spectral band intensities in Figure 4a, it is clear that Basolite® F300 exposes less Lewis acid sites compared to MIL-100(Fe). However, the nature of these Lewis acid sites that both supports expose is very similar.[20] In order to study the Brønsted acidity arising from OH groups coordinating to Fe^{3+} sites, CO probe molecules are adsorbed on the support at 85 K, after drying the sample at 448 K for 3 h at $p < 10^{-3}$ mbar. In both supports, very similar bands at 2165, 2154, and 2138 cm^{-1} appear upon insertion of CO in the cell (Figure 4b and c). Specifically, the bands at 2165 and 2154 cm^{-1} correspond to the CO stretching vibrations interacting with the acidic -OH groups bonded to iron in multimeric species: $[Fe^{3+}–OH_2]\cdots C\equiv O$ and $[Fe^{3+}–OH_2–OH_2]\cdots C\equiv O$, respectively (Figure 4d); while the band at 2137 cm^{-1} corresponds to CO physisorbed in the pores. All in all, from the spectroscopic analysis, it can be deduced that the nature of Brønsted or Lewis acid sites in both Basolite® F300 and MIL-100(Fe) materials is very similar. No significant linker-node under-coordination could be detected for structurally more disordered Basolite® F300, due to the absence of the ν(OH) vibrational band at 3575 cm^{-1}. However, a lower number of Lewis acid sites, could be substantiated for Basolite® F300, as suggested by the lower band intensities across the Py FTIR range from 1000–1080 cm^{-1} for Basolite® F300 compared to MIL-100(Fe).

Hydrophilicity. The differing Lewis acidity for Basolite® F300 and MIL-100(Fe) at the molecular scale could potentially impact the polarity of the materials as a whole, and their hydrophilicity on a more macroscopic level. To evaluate this hydrophilicity, or affinity towards polar molecules, methanol (MeOH) isotherms were collected at 298 K for MIL-100(Fe) and Basolite® F300 (Figure 5 and Figure S3 in Supporting Information). MeOH filling of the pore systems of these materials is in full agreement with N_2 physisorption: the MIL-100(Fe) MeOH isotherm displays two steps resulting from MeOH filling of each cage type; whereas Basolite® F300 shows only one step as a result of the filling of a monomodal pore system.

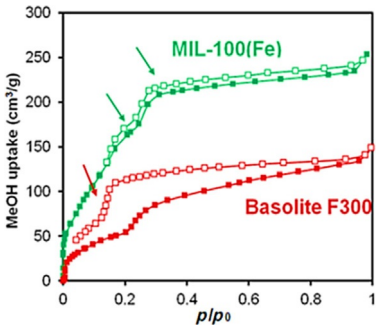

Figure 5. MeOH sorption isotherm acquired at 298 K of both supports. Before adsorption measurement, both samples were degassed at 443 K for 16 h under secondary vacuum ($p < 10^{-3}$ bar). Arrows indicate different steps corresponding to the filling of each type of pore (2 for MIL-100(Fe) and 1 for Basolite® F300).

Second, hydrophilicity of each material can be obtained by Henry's constant from the MeOH isotherms as reported in literature (see Supporting Information Section 3 and Figure S4).[21] For MIL-100(Fe) and Basolite® F300, Henry's constant values are 4.2×10^{-6} and 2.2×10^{-6} mol g^{-1} Pa^{-1}, respectively, evidencing a more hydrophilic surface for MIL-100(Fe) than for Basolite® F300. This is in accordance with the maximal methanol uptake of 253 cm^3 g^{-1} for MIL-100(Fe) compared to 149 cm^3 g^{-1} for Basolite® F300 at $p/p_0 = 0.95$. Even when normalizing to the higher surface area of MIL-100(Fe) relative to Basolite® F300 ($BET_{MIL\text{-}100}/BET_{Basolite} = 1.52$), MIL-100(Fe) adsorbs 12% more MeOH per unit surface area compared to Basolite® F300. This is also the case when normalized to the pore volume of both materials ($V_{p\ MIL\text{-}100}/V_{p\ Basolite} = 1.55$), corresponding to 11% more MeOH adsorbed per unit pore volume.

In the case of MIL-100(Fe), the higher hydrophilicity can be correlated to an increased polarity of the material, induced by Lewis acidity.[22] The higher number of Lewis acid sites for MIL-100(Fe) relative to Basolite® F300 predicts a higher surface polarity and hydrophilicity for MIL-100(Fe). This is indeed confirmed by the MeOH adsorption isotherms, and further suggested by pyridine-probe FTIR experiments. Additionally, thermogravimetric analysis (TGA) was applied to further corroborate the stronger hydrophilicity of MIL-100(Fe); see Figure S4. The results indeed show that MIL-100(Fe) has ≈29 wt.% loss of adsorbed species upon heating to 423 K under Ar flow, corresponding to adsorbed water, in contrast to ≈22 wt.% for Basolite® F300. TGA of both materials under O_2 flow (10 mL min^{-1}) revealed a similar trend, in which the release of adsorbed water and DMF was ≈28 wt.% for MIL-100(Fe) and ≈15 wt.% for Basolite® F300. When comparing the Fe content, calculated from the Fe_2O_3 residue, Basolite® F300 was shown to contain 18.9 wt.% Fe, in contrast to MIL-100(Fe), for which only 15.4 wt.% Fe was observed. These minor differences may correspond to nanosized impurity deposits undetectable by other techniques, as previously found in the literature.[23] Bulk composition, crystal morphology, and surface composition and oxidation states were studied by elemental analysis (Table 1), scanning electron microscopy (SEM) micrographs (Figure S6), and X-ray photoelectron spectroscopy (XPS) (Supporting Information, Section 6 and Figure S7, S8, and S9), respectively, showing very similar properties for both type of materials.

Table 1. Physicochemical properties of FeBTC support materials.

Parameter	Basolite® F300	MIL-100(Fe)
Composition (activated)	unknown	$Fe_3(\mu_3\text{-}O)(C_6H_4O_4)_3)X_3(H_2O)_3{\cdot}n\,H_2O$ ($X = NO_3^-$ or OH^-)
Structure	disordered	crystalline
Space group	-	$F\bar{3}dm$
Fe–O bond length [Å][a]	2.12	2.08
Brønsted acid sites[c,b,f]	$Fe^{3+}{\cdots}OH_2$	$Fe^{3+}{\cdots}OH_2$
Lewis acid sites[c]	Fe^{3+}/Fe^{2+}	Fe^{3+}/Fe^{2+}
MeOH uptake [cm^3 g^{-1}][d]	149	253
K_H (MeOH)[d]	2.2×10^{-6}	4.2×10^{-6}
N_2 BET area [m^2 g^{-1}][e]	685	1040
Pore volume [cm^3 g^{-1}][e]	0.29	0.45
Fe content [%][f,g]	3.9 (19.6)	4.8 (20.3)
C content [%][f,g]	63.7 (37.0)	59.4 (37.7)
O content [%][f,g]	32.1 (n.a.)	35.8 (n.a.)
Adsorbed species [wt.%][h]	22	29

[a] Obtained from X-ray total scattering. [b] Measured with Py-probed, [c] and CO-probed FTIR spectroscopy. [d] Calculated from MeOH sorption isotherm at 298 K; [e] and N_2 sorption isotherm at 77 K. [f] Surface composition determined from XPS survey spectra. [g] Values in brackets correspond to bulk elemental composition in wt.% determined by elemental analysis of the materials combusted with V_2O_5. [h] Obtained from the TGA analysis.

Metal deposition

When used as a catalyst support, the differing structural and (physico-)chemical properties of MIL-100(Fe) and Basolite® F300 can influence the processes involved in metal NP deposition, including solvent wetting, metal precursor adsorption, NP formation/activation, and stability. Below, two archetypal metal deposition methods—colloidal synthesis (Figure 6) and incipient wetness impregnation (Figure 7)—have been applied to illustrate the potential impact of the MOF support properties on the formation of NP-supported catalysts.

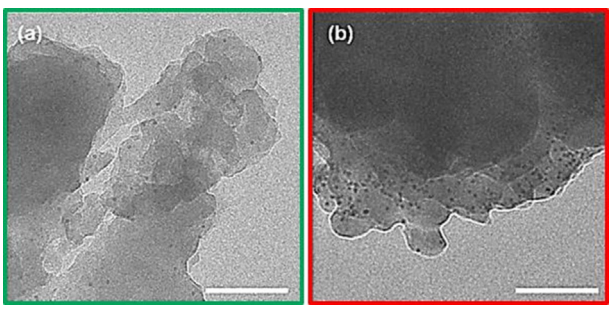

Figure 6. TEM images of the Pd/MOF composites obtained by depositing colloidal metal nanoparticles on (a) MIL-100(Fe) and (b) Basolite® F300. Scale bar represents 100 nm.

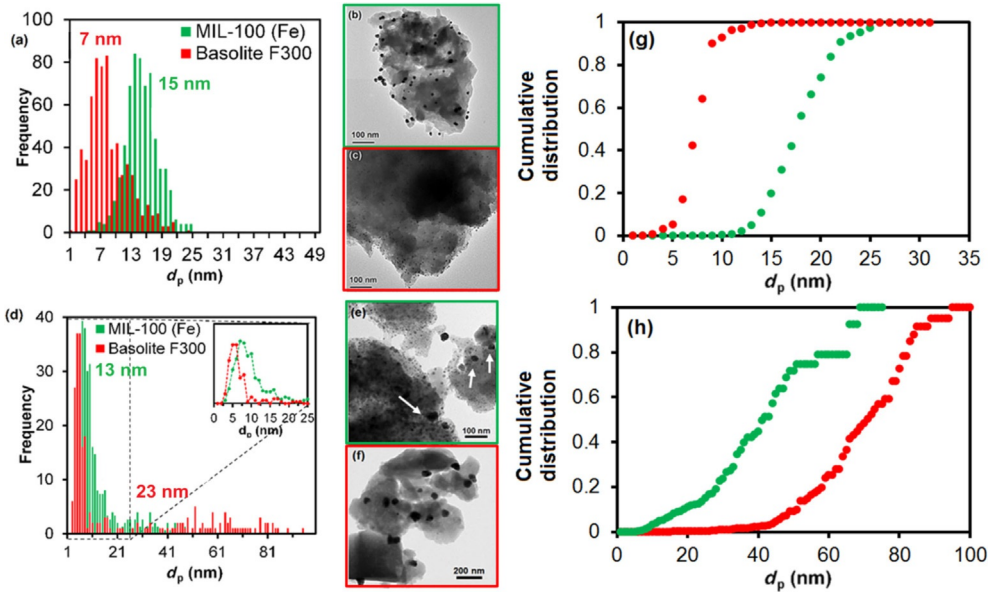

Figure 7. (a) Nanoparticle size distribution (PSD) for both supports. TEM images of 1 wt.% Pd particles supported on (b) MIL-100(Fe) and (c) Basolite® F300 prepared with $Pd(acac)_2$ in chloroform. (d) PSD of the same supports with 1 wt.% Pd using Na_2PdCl_4 in water as a precursor. Inset shows the shape of both distributions for small Pd clusters. TEM images of (e) MIL-100(Fe) and (f) Basolite® F300. The white arrows indicate larger Pd aggregates observed. PSD were calculated from at least 150 particles from TEM images. Cumulative volumetric distribution plots of Pd obtained from (g) $Pd(acac)_2$ and (h) Na_2PdCl_4 precursors.

Colloidal Pd NPs. Oleylamine-stabilized monodisperse 5 nm Pd nanocrystals (Figure S10) were synthesized and deposited on the external surface of MIL-100(Fe) and Basolite® F300 in methanol solution. After stirring the colloidal NPs with the MOF support and carefully washing the excess of surfactant, Pd dispersion on surface was studied by means of transmission electron microscopy (Figure 6).

TEM evidences that the Basolite® F300 support surface is decorated with abundant Pd nanoparticles, whereas in the case of MIL-100(Fe) a lower amount of Pd NPs are observed.

Indeed, bulk elemental analysis shows a higher colloidal uptake of Pd for the Basolite® F300 support (0.256 wt.%) when compared to MIL-100(Fe) (0.142 wt.%) (Table S1). These results can be rationalized when considering the previously observed support properties: Basolite® F300 is more hydrophobic than MIL-100(Fe) due to its lower Lewis acidity. This hydrophobic nature results in a favorable interaction with apolar oleylamine-capped Pd NPs, leading to attractive forces and consecutive adsorption of the colloidal particles on the Basolite® F300 support. In contrast, for MIL-100(Fe), the apolar oleylamine capping ligands will establish reduced interactions with the more hydrophilic (polar, Lewis acid) support surface, leading to decreased NP anchoring. This might eventually result in an increased deposition of capped Pd nanoparticles on Basolite® F300 compared to MIL-100(Fe), as observed in Figure 6.

Pd NPs by incipient wetness impregnation. In the case of incipient wetness impregnation (IWI), two different cases are investigated: IWI of 1) $Pd(acac)_2$ using (apolar) chloroform as a solvent, and 2) Na_2PdCl_4 using (polar) water on MIL-100(Fe) and Basolite® F300 supports. By calcination and H_2 reduction after impregnation of these Pd precursors, very different Pd nanoparticle size distributions are obtained for MIL-100(Fe) and Basolite® F300 supports, as evidenced by TEM (Figure 7). Structural integrity of the material after introducing the Pd particles was corroborated by PXRD, which shows that the crystallinity was fully retained (Figure S11 in Supporting Information). In the case of the $Pd(acac)_2$-chloroform incipient wetness impregnation, well-dispersed nanoparticles with sizes centered around 7–8 nm decorate the Basolite® F300 support. For the more polar MIL-100(Fe) support, larger ca. 15 nm NPs were obtained after calcination and H_2 reduction of the Pd precursor (Figure 7a–c). In the case of Na_2PdCl_4-water impregnation, the situation is reversed, as the larger Pd particles grow on the surface of Basolite® F300, compared to those found on MIL-100(Fe). Further, in addition to those larger Pd particles (>20–50 nm size clusters) found in Basolite® F300, small NPs are also observed for both Basolite® F300 and MIL-100(Fe) supports, as shown in Figure 7d–f. In order to better understand the distribution of Pd NPs, the volumetrically-weighted cumulative size distribution (Figure 7g–h) was calculated, following [Eq. (1)]:

$$\sum_i \frac{v_i \cdot f_i}{v_i} \qquad (1)$$

where v_i is the volume of Pd particles of diameter d_i, and f_i the frequency, assuming spheres. Figure 7g–h shows that the majority of the Pd atoms reside in large-sized Pd NPs (>60 nm) for Basolite® F300 supports, whereas the majority of Pd atoms is included in smaller NPs (<60 nm) for MIL-100(Fe). X-ray diffractograms corroborate the TEM results, as they show higher Pd NP sizes for Basolite® F300 versus MIL-100(Fe) in the Pd (111) and (200) diffraction peaks (Figure 8).

Even though many parameters play a role in the deposition and formation of Pd NPs, we hypothesize that the described observations can be clarified by favored polar–polar and apolar–apolar interactions. Chloroform is an apolar solvent

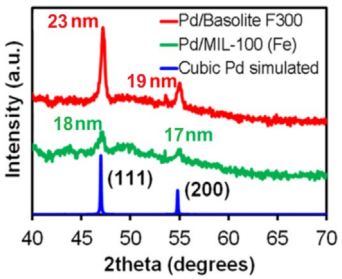

Figure 8. XRD patterns of MOF-supported Pd particles synthesized from the Na_2PdCl_4 anionic precursor in water, dried, and subsequently calcined and reduced. The numbers indicate the estimated crystallite size by the Scherrer equation.

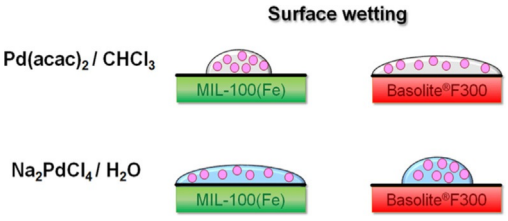

Figure 9. Surface wetting schematic of MIL-100(Fe) and Basolite® F300 when used as supports with different polar vs. apolar combinations of solvent and Pd precursor (depicted as pink circles). Pd precursor aggregates lead to larger particles upon calcination and reduction.

(dipole moment $\bar{D}=1.04$) which interacts attractively with the less polar Basolite® F300, and poorly with the more polar MIL-100(Fe). This will induce differences in solvent wetting of the support, which is more favored on Basolite® F300 (Figure 9). Upon sufficient solvent wetting, the acac-ligands undergo apolar–apolar attractive interactions with the Basolite® F300,[24] resulting in finely dispersed Pd NPs.

In the case of MIL-100(Fe), solvent wetting by chloroform is more limited, which partially prevents intimate interactions between $Pd(acac)_2$ ligands and the support, causing $Pd(acac)_2$ precursor molecules to form larger clusters.[25]

For the case of Na_2PdCl_4-water impregnation, the polar solvent will wet the most polar support, namely MIL-100(Fe), and the polar precursor anions ($PdCl_4^{2-}$) are expected to anchor preferentially on MIL-100(Fe). For more apolar Basolite® F300, solvent wetting will be less favorable, leading to precursor accumulation in the surface and large crystal formation upon calcination and H_2 reduction treatment. We clearly show that although both materials have very similar chemical composition, their surface properties play a key role in adsorption and formation of metal nanoparticles.

Conclusions

Industrial Basolite® F300 and lab-synthesized MIL-100(Fe), with similar iron 1,3,5-benzenetricarboxylate composition, show very different behavior when used as a support for metal nanoparticle synthesis. PXRD and X-ray PDF show that MIL-100(Fe) possess long-range order and has a MTN-zeotype crystal structure, whereas Basolite® F300 lacks long-range order beyond 8 Å. The configurational linker-node disorder responsible for this disordering decreases the number of Lewis acid sites in Basolite® F300 compared to MIL-100(Fe), while the nature of acid sites remains similar. The decreased Lewis acidity of Basolite® F300 induces a change in the polarity/hydrophilicity of the materials, making Basolite® F300 more hydrophobic compared to hydrophilic MIL-100(Fe), as confirmed by methanol adsorption experiments. This discrepancy in hydrophilicity strongly alters the wettability of the solvent, depending on its polar nature, and subsequent precursor anchoring on the support surface. It is shown for archetypal colloidal synthesis and incipient wetness impregnation methods that the intricate nature of iron 1,3,5-benzenetricarboxylate supports can have a strong impact on metal nanoparticle deposition and the eventual nanoparticle size distribution. Alternatively, tuning the MOF structure and function could yield a means to control metal nanoparticle properties and their concomitant catalytic performance.

Experimental Section

Materials synthesis

MIL-100(Fe) $[Fe_3(\mu_3\text{-}O)(C_6H_4O_4)_3)X_3(H_2O)_3{\cdot}nH_2O$ ($X=NO_3^-$ or OH^-, $n\approx11$–14)] was synthesized as described in literature.[26] In brief, iron nitrate nonahydrate ($Fe(NO_3)_3{\cdot}9H_2O$, Sigma–Aldrich, $\geq$99.999%, 33.7 g, 0.08 mol) and 1,3,5-benzenetricarboxylate (H_3BTC, $C_9H_6O_6$, Sigma–Aldrich, $\geq$99%, 15.8 g, 0.08 mol) were mixed in 50 mL of water in a 100 mL round-bottom flask equipped with a reflux condenser. The mixture was heated at 368 K for 24 h and stirred at 300 rpm. Then the orange powder was recovered by centrifugation and washed thoroughly with water and ethanol (VWR International, $\geq$96%). Basolite® F300 was purchased from Sigma–Aldrich. In order to remove trapped unreacted H_3BTC and other impurities, both MOFs were soaked in *N*,*N*-dimethylformamide (C_3H_7NO, DMF, Sigma–Aldrich, $\geq$98%) at 353 K for 12 h. The solvent was then removed and replaced by a 68 mM ammonium fluoride (NH_4F, Sigma–Aldrich, $\geq$98%) aqueous solution at 353 K for 6 h. Then, the powders were recovered by centrifugation and dried in an oven at 393 K in air for 16 h.

Impregnation of Pd precursors

Prior to the solution infiltration of the Pd precursor, the materials were activated in vacuum at 423 K for 12 h and kept in the flask during the addition. The corresponding amount of palladium (II) 2,4-pentanedionate ($Pd(acac)_2$, Sigma–Aldrich, $\geq$99%) to attain 1 wt.% Pd was dissolved in chloroform ($CHCl_3$, Sigma–Aldrich, 99%, anhydrous) and infiltrated into the degassed pores of the materials by adding it dropwise to the powder at room temperature and with constant stirring. The materials were then dried at 298 K for 24 h in Ar and then calcined at 423 K with a heat ramp of 2 K min^{-1}, for 2 h in a N_2 flow of 50 mL min^{-1}, after which the gas feed was switched to H_2 flow of 50 mL min^{-1} for the reduction, and the temperature kept constant for 2 h more, then cooled down to room temperature naturally. No specific passivation method was used. In the case of sodium (II) tetrachloropalladate (Na_2PdCl_4, Sigma–Aldrich, $\geq$99%), the corresponding amount to attain 1 wt.% Pd was dissolved in deionized water. The MOF supports were degassed as described previously and the Pd solution

added to the powder dropwise while stirring under vacuum. The impregnated powder was then dried at room temperature in Ar atmosphere for 16 h and calcined at 423 K for 2 h in a N_2 flow of 50 mL min^{-1} with a heat ramp of 2 K min^{-1}, after which the gas feed was switched to H_2 flow of 50 mL min^{-1}, and the temperature kept constant for 2 h more, then cooled down to room temperature naturally. No specific passivation method was used.

Synthesis and deposition of colloidal Pd nanocrystals

Colloidally stabilized Pd nanocrystals were prepared as described in literature.[27] To deposit the Pd nanocrystals, 0.1 g of MOF was mixed under magnetic stirring with 10 mL of methanol at room temperature. Then, a suspension containing 66.6 mg of colloidal Pd in 5 mL of methanol was added dropwise to the MOF suspension, and the mixture stirred for 24 h at 298 K. Thereafter, the powder was recovered by centrifugation, washed with 10 mL of methanol, separated and carefully washed with 10 mL of *n*-hexane (Sigma–Aldrich, 99.9%) in order to remove the excess of oleylamine (Sigma–Aldrich, $\geq$98%), as seen by the solution turning black. The solid composites were then dried at 353 K in air for 5 h, and stored in air for further analysis.

Materials characterization

Powder X-ray diffraction (PXRD) were obtained by a Bruker-AXS D2 Phaser powder X-ray diffractometer in Bragg–Brentano geometry, using $Co_{K\alpha_{1,2}} = 1.79026$ Å, operated at 30 kV. Measurements were carried out between 5 and 70° using a step size of 0.05° and a scan speed of 1 s. Simulated patterns were obtained by processing the corresponding CIF files with Mercury 3.7® ($\lambda = 1.79026$ Å, FWHM = 0.2).

X-ray total scattering pair distribution functions (X-ray PDF) measurements were performed using powder samples of Basolite® F300 and MIL-100(Fe) that were loaded in 0.5 mm borosilicate capillaries and mounted on a PANalytical Empyrean diffractometer equipped with a Mo X-ray tube ($\lambda = 0.71$ Å, $Q_{max} = 17.7$ Å^{-1}), Mo focusing mirror, and scintillation point detector. Divergence 1°, antiscatter 1/4°, and Soller (0.04 rad) slits were used to adjust the incident beam profile; a programmable receiving slit, set to a height of 1 mm, was used for the diffracted beam. Total scattering data were collected over the angular range $2.75 > 2\theta > 140°$, yielding data with useable $Q_{max} = 15$ Å^{-1}. These data were corrected for background, Compton, and multiple scattering and beam attenuation by the sample container using the GudrunX package.[28] The normalized structure factor *F(Q)* was converted to the PDF in the form of the *D(r)* function as defined in ref. [29].

X-ray photoelectron spectroscopy (XPS) experiments were performed by using a Thermo Scientific K-Alpha spectrometer equipped with a monochromatic small-spot X-ray source and a 180° double focusing hemispherical analyzer with a 128-channel delay line detector. Spectra were obtained using an aluminum anode ($Al_{K\alpha} = 1486.6$ eV) operated at 72 W and a spot size of 400 μm. Survey scans and high-resolution scans of the separate regions were measured at constant pass energies of 200 eV and 50 eV, respectively. The background pressure of the ultra-high vacuum (UHV) chamber was 2×10^{-8} mbar. Sample charging was compensated for by the use of an electron flood gun, and binding energy calibration was done by setting the peak as reference for all samples to a binding energy (BE) of 284.8 eV, which corresponds to a combination of phenyl (sp2) and adventitious carbon (sp3), according to previously reported procedures. Fitting of the spectra (BE, FWHM, peak shape, asymmetry, number of species) was carried out with CasaXPS© software, version 2.3.16.

Fourier-transformed infrared (FTIR) spectroscopy measurements were recorded on a PerkinElmer System 2000 instrument (16 scans, 4 cm^{-1} resolution, DTGS detector, cell with KBr windows). The materials were prepared in a press tool by pressing ≈10 mg of powder into self-supported pellets (2 cm^2 area), which were then activated at 448 K for 3 h at $p < 10^{-5}$ mbar. After cooling down the cell with liquid N_2 temperature to 85 K, a 10% CO/He v/v (Linde AG, 99.998% purity) mixture was introduced to an equilibrium pressure of 100 mbar, and was then desorbed stepwise at constant temperature, until reaching total evacuation again at a pressure of ≈10^{-5} mbar. When pyridine (Py) was used as a probe molecule, similar pellets were placed into a cell as the one described above and the spectra recorded with a ThermoFisher Nicolet *i5* spectrometer (32 scans, 4 cm^{-1} resolution, DTGS detector). The pellet was evacuated by heating in a cell at 498 K (ramp of 10 K min^{-1}) for 24 h at $p < 10^{-5}$ mbar, which was then cooled down to 323 K. At that temperature, pyridine (redistilled, 99.9%, Sigma–Aldrich) vapor was introduced into the cell and the equilibrium pressure set to 15 mbar. Spectra were recorded in adsorption mode up to 60 min after introduction of the gas.

Thermogravimetric analysis (TGA) of the samples was done in a PerkinElmer Pyris 1 TGA equipment. A heating ramp of 5 K min^{-1} from 323 to 1073 K under a 10 mL min^{-1} of either O_2 and N_2 atmosphere was used for the analysis.

N_2 adsorption isotherms were measured at 77 K on a Micromeritics ASAP 2010 apparatus. Prior to the measurements, samples were activated at 298 K under primary vacuum until the pressure reached 1 mbar and then switched to secondary vacuum at 443 K for 16 h. The measurement temperature was controlled with liquid N_2 at 77 K. Adsorption equilibrium was assumed when the variation of the cell pressure was 5% for minimum and maximum period of 9 min and 30 min, respectively.

Methanol adsorption isotherms were measured at 298 K on BELmax apparatus (MicrotracBEL). Prior to the measurements, samples were activated to 443 K under secondary vacuum for 16 h. Prior to performing methanol adsorption, methanol (analyte) was flash-frozen with liquid nitrogen and then evacuated under dynamic vacuum 3 times in order to remove dissolved gases from the reservoir. The measurement temperature was controlled with a water bath at 298 K and with the dosing manifold controlled at 313 K to avoid unwanted condensation effects. Helium was used to estimate the dead volume prior to the methanol adsorption-desorption measurements. Adsorption equilibrium was assumed when the variation of the cell pressure was 0.5% for a minimum period of 5 min.

Elemental analysis of the content of Fe, O, and C was measured by atomic absorption spectroscopy (AAS) after combustion of the samples with V_2O_5 at Mikroanalytisches Laboratorium Kolbe (Mülheim an der Ruhr, Germany). In the case of Pd, the samples were atomized by inductively coupled plasma (ICP) and analyzed with atomic emission spectroscopy (AES).

Scanning electron microscopy (SEM) images were recorded on a PhenomPro X microscope operated at 10 kV. The powder samples were supported on carbon tape deposited over Al stubs (FEI stubs) and inserted in the microscope vacuum chamber without Au coating.

Transmission electron microscopy (TEM) images were recorded in the bright-field imaging mode by using a JEOL2011, a Tecnai T12 or a Tecnai T20FEG transmission electron microscope operated at 120 kV (the two former) or 200 kV, respectively. Samples were cast onto holey-carbon coated 300 mesh Cu grids from methanol sus-

pensions. The mean particle size of Pd was calculated from at least 200 different particles observed by using TEM.

Acknowledgements

This project has received funding from the European Union Horizon 2020 research and innovation program under the Marie-Sklodowska-Curie grant agreement 641887 (DEFNET). S. Dissegna (Technical Universtät München, TUM), W. S. Lamme (Utrecht University, UU) and L. C. E. Pompe (UU) are gratefully acknowledged for the TEM measurements. We thank H. C. de Waard (UU) for analysis of the elemental content of metals and carbon in the different samples. B.S. gratefully acknowledges the Netherlands National Science Foundation (NWO) for her personal VENI grant. M.F. gratefully acknowledges the Marie Sklodwoska-Curie program agreement No. 748563. B.M.W. acknowledges financial support from The Netherlands Organisation for Scientific Research (NWO) Gravitation Program (Netherlands Center for Multiscale Catalytic Energy Conversion, MCEC). This project has received funding from the European Research Council (ERC) under the European Union's Horizon 2020 research and innovation program (279705, acronym NANOSTRUCTURE).

Conflict of interest

The authors declare no conflict of interest.

Keywords: Basolite · heterogeneous catalysis · lattice disorder · metal-organic frameworks (MOF) · MIL-100 (Fe) · Pd nanoparticles

[1] a) H. C. Zhou, J. R. Long, O. M. Yaghi, *Chem. Rev.* **2012**, *112*, 673 – 674; b) J. Lee, O. K. Farha, J. Roberts, K. A. Scheidt, S. T. Nguyen, J. T. Hupp, *Chem. Soc. Rev.* **2009**, *38*, 1450 – 1459; c) A. Corma, H. García, F. X. Llabrés, I. Xamena, *Chem. Rev.* **2010**, *110*, 4606 – 4655.

[2] M. Müller, A. Devaux, C. H. Yang, L. De Cola, R. A. Fischer, *Photochem. Photobiol. Sci.* **2010**, *9*, 846 – 853.

[3] G. Li, H. Kobayashi, J. M. Taylor, R. Ikeda, Y. Kubota, K. Kato, M. Takata, T. Yamamoto, S. Toh, S. Matsumura, H. Kitagawa, *Nat. Mater.* **2014**, *13*, 802 – 806.

[4] M. Müller, S. Hermes, K. Kähler, M. W. E. van den Berg, M. Muhler, R. A. Fischer, *Chem. Mater.* **2008**, *20*, 4576 – 4587.

[5] a) C. Rösler, R. A. Fischer, *CrystEngComm* **2015**, *17*, 199 – 217; b) M. Meilikhov, K. Yusenko, D. Esken, S. Turner, G. Van Tendeloo, R. A. Fischer, *Eur. J. Inorg. Chem.* **2010**, *2010*, 3701 – 3714; c) P. Falcaro, R. Ricco, A. Yazdi, I. Imaz, S. Furukawa, D. Maspoch, R. Ameloot, J. D. Evans, C. J. Doonan, *Coord. Chem. Rev.* **2016**, *307*, 237 – 254; d) Q. Yang, Q. Xu, H. L. Jiang, *Chem. Soc. Rev.* **2017**, *46*, 4774 – 4808; e) A. Dhakshinamoorthy, H. Garcia, *Chem. Soc. Rev.* **2012**, *41*, 5262 – 5284; f) H. R. Moon, D.-W. Lim, M. P. Suh, *Chem. Soc. Rev.* **2013**, *42*, 1807 – 1824.

[6] Y. Zhang, Y. Zhou, Y. Zhao, C. J. Liu, *Catal. Today* **2016**, *263*, 61 – 68.

[7] a) D. S. Sholl, R. P. Lively, *J. Phys. Chem. Lett.* **2015**, *6*, 3437 – 3444; b) L. Yuan, M. Tian, J. Lan, X. Cao, X. Wang, Z. Chai, J. K. Gibson, W. Shi, *Chem. Commun.* **2018**, *54*, 370 – 373.

[8] M. J. Cliffe, W. Wan, X. Zou, P. A. Chater, A. K. Kleppe, M. G. Tucker, H. Wilhelm, N. P. Funnell, F. X. Coudert, A. L. Goodwin, *Nat. Commun.* **2014**, *5*, 4176.

[9] T. D. Bennett, A. K. Cheetham, *Acc. Chem. Res.* **2014**, *47*, 1555 – 1562.

[10] a) J. Canivet, M. Vandichel, D. Farrusseng, *Dalton Trans.* **2016**, *45*, 4090 – 4099; b) Z. Fang, B. Bueken, D. E. De Vos, R. A. Fischer, *Angew. Chem. Int. Ed.* **2015**, *54*, 7234 – 7254; *Angew. Chem.* **2015**, *127*, 7340 – 7362; c) T. D. Bennett, A. H. Fuchs, A. K. Cheetham, F. X. Coudert, *Dalton Trans.* **2016**, *45*, 4058 – 4059; d) T. D. Bennett, A. K. Cheetham, A. H. Fuchs, F. X. Coudert, *Nat. Chem.* **2017**, *9*, 11 – 16.

[11] X. Hu, X. Lou, C. Li, Y. Ning, Y. Liao, Q. Chen, E. S. Mananga, M. Shen, B. Hu, *RSC Adv.* **2016**, *6*, 114483 – 114490.

[12] a) M. Sanchez-Sanchez, I. de Asua, D. Ruano, K. Diaz, *Cryst. Growth Des.* **2015**, *15*, 4498 – 4506; b) A. Dhakshinamoorthy, M. Alvaro, H. Garcia, *Chem. Commun.* **2012**, *48*, 11275 – 11288.

[13] L. Sciortino, A. Alessi, F. Messina, G. Buscarino, F. M. Gelardi, *J. Phys. Chem. C* **2015**, *119*, 7826 – 7830.

[14] M. Todaro, A. Alessi, L. Sciortino, S. Agnello, M. Cannas, F. M. Gelardi, G. Buscarino, *J. Spectr.* **2016**, *2016*, 1.

[15] P. Horcajada, S. Surble, C. Serre, D. Y. Hong, Y. K. Seo, J. S. Chang, J. M. Greneche, I. Margiolaki, G. Ferey, *Chem. Commun.* **2007**, 2820 – 2822.

[16] a) J. Shi, S. Hei, H. Liu, Y. Fu, F. Zhang, Y. Zhong, W. Zhu, *J. Chem.* **2013**, 792827; b) S. Huang, K. L. Yang, X. F. Liu, H. Pan, H. Zhang, S. Yang, *RSC Adv.* **2017**, *7*, 5621 – 5627; c) F. Tan, M. Liu, K. Li, Y. Wang, J. Wang, X. Guo, G. Zhang, C. Song, *Chem. Eng. J.* **2015**, *281*, 360 – 367.

[17] H. Leclerc, A. Vimont, J. C. Lavalley, M. Daturi, A. D. Wiersum, P. L. Llwellyn, P. Horcajada, G. Ferey, C. Serre, *Phys. Chem. Chem. Phys.* **2011**, *13*, 11748 – 11756.

[18] J. W. Yoon, Y. K. Seo, Y. K. Hwang, J. S. Chang, H. Leclerc, S. Wuttke, P. Bazin, A. Vimont, M. Daturi, E. Bloch, P. L. Llewellyn, C. Serre, P. Horcajada, J. M. Grenèche, A. E. Rodrigues, G. Férey, *Angew. Chem. Int. Ed.* **2010**, *49*, 5949 – 5952; *Angew. Chem.* **2010**, *122*, 6085 – 6088.

[19] K. N. Wong, S. D. Colson, *J. Mol. Spectrosc.* **1984**, *104*, 129 – 151.

[20] A. Dhakshinamoorthy, M. Alvaro, P. Horcajada, E. Gibson, M. Vishnuvarthan, A. Vimont, J. M. Grenèche, C. Serre, M. Daturi, H. Garcia, *ACS Catal.* **2012**, *2*, 2060 – 2065.

[21] J. Canivet, J. Bonnefoy, C. Daniel, A. Legrand, B. Coasne, D. Farrusseng, *New J. Chem.* **2014**, *38*, 3102 – 3111.

[22] a) S. Dissegna, R. Hardian, K. Epp, G. Kieslich, M. V. Coulet, P. Llewellyn, R. A. Fischer, *CrystEngComm* **2017**, *19*, 4137 – 4141; b) D. Farrusseng, S. Aguado, C. Pinel, *Angew. Chem. Int. Ed.* **2009**, *48*, 7502 – 7513; *Angew. Chem.* **2009**, *121*, 7638 – 7649.

[23] Y. K. Seo, J. W. Yoon, J. S. Lee, U. H. Lee, Y. K. Hwang, C. H. Jun, P. Horcajada, C. Serre, J. S. Chang, *Microporous Mesoporous Mater.* **2012**, *157*, 137 – 145.

[24] D. Esken, X. Zhang, O. I. Lebedev, F. Schroder, R. A. Fischer, *J. Mater. Chem.* **2009**, *19*, 1314 – 1319.

[25] M. L. Toebes, J. A. van Dillen, K. P. de Jong, *J. Mol. Catal. A* **2001**, *173*, 75 – 98.

[26] F. Zhang, J. Shi, Y. Jin, Y. Fu, Y. Zhong, W. Zhu, *Chem. Eng. J.* **2015**, *259*, 183 – 190.

[27] S. W. Kim, J. Park, Y. Jang, Y. Chung, S. Hwang, T. Hyeon, Y. W. Kim, *Nano Lett.* **2003**, *3*, 1289 – 1291.

[28] A. K. Soper, Tech. Rep. RAL-TR-2011-013 Rutherford Appleton Laboratory **2011**.

[29] D. Keen, *J. Appl. Crystallogr.* **2001**, *34*, 172 – 177.

Manuscript received: February 10, 2018
Version of record online: April 30, 2018

